Supplementary Information

# Vertically-stacked monolithic multilayer perovskite photodetectors for color-filter-free imaging

Sergey Tsarev[1,2], Daria Proniakova[1], Erfu Wu[1,3], Gebhard Matt[1,2], Kostiantyn Sakhatskyi[1,2], Lorenzo Ferraressi[1,3], Liu Xuqi[1], Radha Kothandaraman[2], Fan Fu[2], Ivan Shorubalko[3], Sergii Yakunin[1,2], Maksym V. Kovalenko[1,2]

[1] Laboratory of Inorganic Chemistry, Department of Chemistry and Applied Biosciences, ETH Zürich, CH-8093 Zürich, Switzerland

[2] Laboratory for Thin Films and Photovoltaics, Empa – Swiss Federal Laboratories for Materials Science and Technology, CH-8600 Dübendorf, Switzerland

[3] Transport at Nanoscale Interfaces Laboratory, Empa – Swiss Federal Laboratories for Materials Science and Technology, CH-8600 Dübendorf, Switzerland

[*]E-mail: mvkovalenko@ethz.ch; yakunins@ethz.ch

## Contents


Supplementary Note 1. Perovskite sensor structure ..... 3

1.1 Red color detector stack ..... 3

1.2 Green color detector Stack ..... 3

1.3 Blue color detector stack ..... 4

Supplementary Table 1. Complete sensor structure 1. ..... 4

Supplementary Table 2. Complete sensor structure 2 ..... 5

Supplementary Note 2. Alternative technologies promising for monolithic stacked detector fabrication ..... 8

2.1 III-V materials for integration in vertically stacked photodetectors. ..... 9

2.2 Organic photodetectors ..... 12

Supplementary Note 3. Procedure for evaluation of color accuracy of optical sensor ..... 16

Supplementary Fig. 1 | Atomic force microscopy images of perovskite layers. ..... 18

Supplementary Fig. 2 | External Quantum Efficiency of a stacked detector with structure 1 .. 19

Supplementary Fig. 3 | 3 dB bandwidth of the R, G, and B single color detectors. ..... 19

Supplementary Fig. 4 | Capacitance vs frequency measurements of stacked photodetectors. . 20

Supplementary Fig. 5 | Emission spectra of RGB channels emitted by LC-10W diode. ..... 20

Supplementary Fig. 6 | Comparative performance of red detectors with 30 nm and 100 nm bottom gold electrode. ..... 21

Supplementary Table 4. Comparative detectivity metrics of broadband perovskite, organic, silicon, and stacked perovskite photodetectors ..... 8

Supplementary References ..... 22

## Supplementary Note 1. Perovskite sensor structure

### 1.1 Red color detector stack

In our approach to developing a stacked perovskite layer, we aimed for methodologies designed for seamless transfer to CMOS-compatible processing. We selected vapor-phase perovskite deposition to facilitate deposition on textured and uneven surfaces, which may be essential for further application on CMOS chips and avoid problems with the dissolution of perovskites by the subsequent layers. We avoided thick dielectric spacers, such as polymer films and parylene, to maintain a relatively thin total sensor thickness. This is vital for future developments of the practical sensor arrays, which will require lithographic etching and integrating via connectors onto CMOS chips.

The deposition process begins with dielectric/Au/dielectric electrodes, utilizing $MoO_3$ as an adhesive layer beneath the gold and as a buffer layer. This reflective Au electrode was used to enhance the light absorption in the red detection layer. We discovered that keeping the gold layer thin (30 nm) was essential for achieving leak-free detectors, as devices with 100nm gold layers exhibited significantly higher leakage (Supplementary Fig. 6). In general, these stacked structures are very demanding of having sharp-edge-free bottom electrodes. We chose $MAPbI_2Br$ for its ease of use and reproducibility as the perovskite composition. The structure was completed with a C60/ZnO/ITO layer, employing ZnO as a protective layer to mitigate sputter damage on the perovskite/ETL stack. Continuing the fabrication, we deposited dielectric stacks. It was noted that while the main ITO electrode surface was sufficiently protective against perovskite decomposition during processing, areas not covered by ITO (deposited through a shadow mask) might react with subsequent perovskite layer stacks. Initially, a combination of $SnO_2$ and $SiO_2$ was included as protective and dielectric layers. The $SnO_2$ layer (deposited with pulsed DC sputtering) was later selected due to observed degradation and bleaching of perovskite when $SiO_2$ was sputtered (RF) directly onto areas of the perovskite substrate without ITO coverage.

### 1.2 Green color detector Stack

The green stack's fabrication commenced with the deposition of the ITO electrode and a $SnO_2$/C60 ETL stack. We selected $CsPbBr_2I$ as a stable inorganic perovskite for the perovskite layer. We encountered low batch-to-batch reproducibility while experimenting with the thermally evaporated $MAPbBr_{2.5}I_{0.5}$ composition. Given the entire sensor fabrication process could extend

up to 3-4 weeks, maintaining high reproducibility was deemed crucial, leading to a focus on inorganic perovskites. A composite HTL comprising TCTA/$MoO_3$ and an additional AZO nanocrystal buffer layer was used to minimize the sputtering damage on the green cell. The TCTA layer was chosen to maintain vapor deposition for the entire stack and its high glass transition temperature[1], crucial for the thermal stability of the cell upon deposition of the third stack.

### 1.3 Blue color detector stack

The fabrication of the blue stack began with the deposition of a 2PACz and NiO composite layer. The initial 2PACz coating provided a hole-selective interface coating for the edges of the bottom ITO electrode, addressing the potential non-conformality of NiO NC coating on the sharp electrode edges. The $CsPbClBr_2$ layer was used as the absorber layer due to its high stability. Although we experimented with $MAPbBr_{1.5}Cl_{1.5}$ as an absorber layer, we could not achieve an EQE higher than 20% with this composition. Notably, we achieved an 81% EQE with high-performance solution-processed $FAPbBr_{1.5}Cl_{1.5}$ detectors. However, the evaporation of FABr or FACl precursors in our PVD chamber proved challenging. To maintain consistency with PVD-processed stacks, we decided against incorporating any solution-processed perovskite layers in the stack, further complicated by issues of perovskite dissolution in the bottom layers when a solution-based composition was used.

**Supplementary Table 1. Complete sensor structure 1.** Layers are deposited in order from layer 1, beginning with a 25x25 mm soda lime glass substrate.

| | Layer | Nominal thickness (nm) | Deposition method | Role |
|---|---|---|---|---|
| 1 | $MoO_3$ | 15 | Thermal evaporation | Adhesion |
| 2 | Gold | 30 | Thermal evaporation | Electrode |
| 3 | $MoO_3$ | 30 | Thermal evaporation | Buffer |
| 4 | 2PACz | <2 | Spincoating | Hole-selective |
| 5 | $MAPbBrI_2$ | 450 | Thermal evaporation | Absorber |
| 6 | C60 | 20 | Thermal evaporation | Electron-transport |

| | | | | |
|---|---|---|---|---|
| 7 | ZnO | 40 | Spincoating | Buffer |
| 8 | ITO | 180 | Sputtering | Electrode |
| 9 | $SnO_2$ | 40 | Sputtering | Protective |
| 10 | $SiO_2$ | 200 | Sputtering | Dielectric |
| 11 | ITO | 180 | Sputtering | Electrode |
| 12 | $SnO_2$ | 40 | Sputtering | Electron-transport |
| 13 | C60 | 5 | Thermal evaporation | Electron-transport |
| 14 | $CsPbBr_2I$ | 300 | Thermal evaporation | Absorber |
| 15 | TCTA | 15 | Thermal evaporation | Hole-transport |
| 16 | $MoO_3$ | 30 | Thermal evaporation | Buffer |
| 17 | AZO | 40 | Spincoating | Buffer |
| 18 | ITO | 140 | Sputtering | Electrode |
| 19 | $SnO_2$ | 40 | Sputtering | Protective |
| 20 | $SiO_2$ | 200 | Sputtering | Dielectric |
| 21 | ITO | 100 | Sputtering | Electrode |
| 22 | 2PACz | <2 | Spincoating | Hole selective |
| 23 | NiO | 30 | Spincoating | Hole transport |
| 24 | TCTA | 5 | Thermal evaporation | Hole transport |
| 25 | $CsPbBr_2Cl$ | 200 | Thermal evaporation | Absorber |
| 26 | PCBM | ~40 | Spincoating | Electron-transport |
| 27 | C60 | 5 | Thermal evaporation | Electron-transport |
| 28 | ZnO | 40 | Spincoating | Buffer |
| 29 | ITO | 120 | Sputtering | Electrode |

**Supplementary Table 2. Complete sensor structure 2.** Layers are deposited in order from layer 1, beginning with a 25x25 mm soda lime glass substrate.

| Layer | Nominal thickness (nm) | Deposition method | Role |
|---|---|---|---|

| | | | | |
|---|---|---|---|---|
| 1 | $MoO_3$ | 15 | Thermal evaporation | Adhesion |
| 2 | Gold | 30 | Thermal evaporation | Electrode |
| 3 | $MoO_3$ | 30 | Thermal evaporation | Buffer |
| 4 | 2PACz | <2 | Spincoating | Hole-selective |
| 5 | $MAPbBrI_2$ | 450 | Thermal evaporation | Absorber |
| 6 | C60 | 40 | Thermal evaporation | Electron-transport |
| 7 | ZnO | 40 | Spincoating | Buffer |
| 8 | $SnO_2$ | 40 | ALD | Buffer |
| 9 | ITO | 180 | Sputtering | Electrode |
| 10 | $SnO_2$ | 40 | Sputtering | Electron-transport |
| 11 | C60 | 5 | Thermal evaporation | Electron-transport |
| 12 | $CsPbBr_2I$ | 300 | Thermal evaporation | Absorber |
| 13 | TCTA | 15 | Thermal evaporation | Hole-transport |
| 14 | $MoO_3$ | 30 | Thermal evaporation | Buffer |
| 15 | ITO | 100 | Sputtering | Electrode |
| 16 | 2PACz | <2 | Spincoating | Hole selective |
| 17 | NiO | 30 | Spincoating | Hole transport |
| 18 | TCTA | 5 | Thermal evaporation | Hole transport |
| 19 | $CsPbBr_2Cl$ | 400 | Thermal evaporation | Absorber |
| 20 | C60 | 20 | Thermal evaporation | Electron-transport |
| 21 | BCP | 8 | Thermal evaporation | Buffer |
| 22 | Ag | 1 | Thermal evaporation | Adhesive layer |
| 23 | ZnO | 40 | Spincoating | Buffer |
| 24 | ITO | 120 | Sputtering | Electrode |

In **structure 2**, we implemented the following modifications: a buffer layer of ALD $SnO_2$ was added to enhance the protection of the red cell from the layers above. It was determined that using a conformal protection layer avoids the need for a dielectric layer, which, in turn, contributed to an increase in the EQE of the red cell. For the green cell, it was found that incorporating an AZO nanocrystal buffer layer significantly compromised the environmental stability of the sensors,

which would be crucial for further integration into CMOS as most of the conventional clean-room processes occur under ambient conditions. Furthermore, we removed dielectrics in the stack to minimize optical losses and simplify the fabrication.

The blue cell structure underwent a complete redesign, replacing the $CsPbBr_2Cl$ uniform film with a gradient-grown film, utilizing the deposition of CsCl at a higher rate initially. These films exhibited a significantly higher EQE than those with uniform growth, enabling us to achieve a peak EQE of 54% in a top-illuminated structure. As for the ETL, a combination of C60/BCP/Ag/ZnO layers was found to outperform pure C60/ZnO, likely due to enhanced hole blocking and improved protection of the perovskite layer from sputter damage.

**Supplementary Table 3. Comparative detectivity metrics of broadband perovskite, organic, silicon, and stacked perovskite photodetectors**

| **Detector** | **D (Jones)** | **Reference** |
|---|---|---|
| Stacked - blue | $2\times10^{10}$ | Our work |
| Stacked - green | $8.6\times10^{10}$ | Our work |
| Stacked - red | $1.5\times10^{11}$ | Our work |
| State-of-the-art broadband perovskite detectors | | |
| PTAA/$MAPbI_3$/$C_{60}$ | $7.8 \times 10^{12}$ | [2] |
| $TiO_2$/$Al_2O_3$/PCBM/$MAPbI_3$/Spiro/Au | $4 \times 10^{12}$ | [3] |
| $NiO_x$:$PbI_2$/$MAPbI_3$/$C_{60}$ | $4.0 \times 10^{12}$ | [4] |
| Silicon detectors | | |
| FDS1010 (Thorlabs) | $4.8 \times 10^{12}$ at $1cm^2$ (20 V) | [5] |
| FDS100 (Thorlabs) | $3 \times 10^{13}$ at 13 $mm^2$ (5 V) | [5] |
| 818-BB-45 (Hamamatsu) | $1.1\times10^{12}$ at 1.1 $mm^2$ | [6] |
| Organic photodetectors | | |
| PCDTBT:$PC_{71}BM$ | $1.8 \times 10^{12}$ (− 1 V) | [7] |
| P3HT:PTB7: $PC_{71}BM$ | $1.1 \times 10^{12}$ (0 V) | [8] |
| PBTTT:$PC_{61}BM$ | $3.6 \times 10^{12}$ (0 V) | [9] |

## Supplementary Note 2. Alternative technologies promising for monolithic stacked detector fabrication

While perovskite absorber materials hold potential for monolithic stacked detector fabrication, it is important to note that this technology is not restricted to specific absorber materials. Any photosensitive materials possessing appropriate bandgap and transparency characteristics can

potentially serve as a viable option for color sensors. Alongside perovskite, we consider two classes of materials with tuneable bandgaps that hold promise for vertical stacking: III-V semiconductors and bulk heterojunction organic semiconductors. These material families have been extensively employed in tandem solar cells, which share a fundamentally similar architectural framework with stacked diode sensors. This note discusses existing technologies of III-V and organic semiconductors within the context of stacked detector applications.

**2.1 III-V materials for integration in vertically stacked photodetectors.**

Epitaxially grown III-V alloys offer superior optoelectronic materials characterized by a wide range of tunable bandgaps, as evidenced by numerous ultra-high-efficiency multijunction solar cells employed in concentrator and space applications[10,11]. Generally, the primary concern associated with III-V semiconductors is their cost, rendering them primarily suitable for niche applications that demand high performance and tolerate higher costs, such as space energy sources[12], ultra-high bandwidth detectors[13,14], and concentrator solar cells[10,15,16]. Notably, recent advancements, particularly the adoption of an ultrasonic lift-off technique, have substantially mitigated costs by enabling substrate reuse, achieving a cost reduction of 4-6 times compared to traditional molecular beam epitaxy (MBE) growth techniques[17]. However, despite these cost reductions, lattice matching between film and substrate remains a critical factor in epitaxial growth processes, also influencing the performance of resulting devices[10,11,18]. Here, we will address the primary III-V materials suitable for detecting colors within the visible spectrum, particularly those that align with the RGB color range. The summary of these findings is shown in Supplementary Table 4

*2.1.1. Gallium-indium phosphide based materials*

$Ga_xIn_{1-x}P$ is utilized in the top and middle junction cells for terrestrial concentrator applications due to its tuneable bandgap ranging from approximately 1.68 to 1.93 eV[18,19]. This range of bandgaps renders it suitable for use in red color detector pixels. The material is commonly employed as a top cell component in tandem multijunction cells yielding 47.6% efficient solar cells in 2022[16]. Typically, the growth of this material is confined to lattice-matching substrates such as GaAs wafers, as lattice mismatch can lead to a decrease in performance due to a high density of lattice dislocations at the interface with the substrate[20]. It has been noted that obtaining

high-quality $Ga_xIn_{1-x}P$ is comparatively easier than $Al_xGa_{1-x}As$ due to the latter's strong affinity for the formation of Al-O defects during growth[21].

$Al_xGa_yIn_{1-x-y}P$ is employed in multijunction devices as a top cell component of tandem multijunction cells, typically grown directly on GaAs wafers or films interconnected via a tunnel junction, as reported in a recent paper highlighting solar cells with the second-highest performance at 47.1[10] from NREL. If we extrapolate the geometry of this top-performing multijunction cell to the photodetector context, then the top two junctions, with bandgaps of 1.7 eV ($Al_xGa_{1-x}As$) and 2.1 eV, can potentially be utilized for red and green color detection, respectively, based on light absorption considerations.

However, the majority of reported phosphide and arsenide materials, which are direct bandgap semiconductors, typically have bandgaps reaching up to 2.38 eV, slightly below the approximately 2.5 eV bandgap[22] required to maintain selectivity to blue light. Given that most absorbers in tandem solar cells do not utilize such wide bandgap materials, it becomes necessary to integrate a different material specifically tailored for blue light detection.

*2.1.2. Gallium nitride and indium gallium nitride based materials*

GaN-based nitride semiconductors have significantly advanced the development of optoelectronic devices, particularly laser diodes, LEDs, and UV photodetectors. The bandgap of gallium nitride (GaN) can be tuned by incorporating indium nitride (InN), resulting in the formation of $InxGa_{1-}$xN semiconductors. This modification allows for a variable bandgap that extends from 3.42 eV, characteristic of pure GaN, down to 1.7 eV. Furthermore, it is suggested that the bandgap could be reduced to as low as 0.64 eV with the use of pure InN[23,24]. However, achieving uniform bandgap tunability is challenging due to the difference in lattice spacing between InN and GaN[25]. The lattice mismatch between these materials presents obstacles in the growth of mixed $In_xGa_{1-x}N$ films, although this challenge can be mitigated by utilizing GaN or AlN buffer layers as templates[26]. Furthermore, InxGa1-xN tends to exhibit n-type semiconductivity and must be doped to form p-n junctions for photodiodes. This process is hindered by the necessity to generate a high density of defects for p-doping to compensate for an excess of electrons in the material[27]. Nonetheless, $In_xGa_{1-x}N$ has emerged as a promising material for blue light detection in photodetectors[13,28,29], and micro-detector arrays[14], demonstrating high responsivity (.29 A/W at 400nm[14]) and low dark current detectors. Moreover, direct integration of $In_xGa_{1-x}N$ on Si via a buffer GaN layer has been

demonstrated[13]. Additionally, there have been successful attempts towards integrating $Al_xGa_yIn_{1-x-y}P$ and $In_xGa_{1-x}N$ in dual-band LEDs, showcasing potential for their successful incorporation into multiband color detectors[30].

When it comes to detecting green light, it has been observed that as the band gap decreases, $In_xGa_{1-x}N$ experiences greater susceptibility to phase separation and high defect concentrations, resulting in poor color selectivity and increased leakage in devices [31]. Reports on green-light detection using $In_xGa_{1-x}N$ are scarce[31], potentially due to its performance significantly lagging behind silicon performance with optical filters. Nevertheless, there are reports of existing multijunction solar cells employing $In_xGa_{1-x}N$ in conjunction with silicon, offering promise for the potential integration of this material as a middle layer in Si (red)/$In_xGa_{1-x}N$ (green)/ $In_yGa_{1-y}N$ (blue) configurations[32]. However, thus far, only a 60% external quantum efficiency (EQE) has been demonstrated for $In_xGa_{1-x}N$[32], and research in this field remains relatively inactive.

*2.1.3. Summary for III-V photodetectors*

To sum up, a potentially viable sensor multistack comprising only III-V semiconductors as absorbers would entail lattice-matched $Ga_xIn_{1-x}P$ or $Al_xGa_{1-x}As$ for red and $Al_xGa_yIn_{1-x-y}P$ for green detection layers, respectively, integrated with an $In_xGa_{1-x}N$ layer via a GaN buffer layer. Achieving a sufficiently low degree of lattice mismatch between the nitride and phosphide/arsenide components would be crucial, possibly necessitating separate deposition of blue and R-G detectors and employing a lift-off transfer process for the former. However, even if successful, questions remain regarding how to pattern and make electrical contacts to this structure. For this purpose, one can deposit a transparent conductive oxide electrode, which, however, will interfere with the epitaxial growth of absorber layers on top of this layer. Alternatively, if heavily doped contacts are used, it is not apparent how feasible is to dope them and electrically separate them from the main stack to obtain a low-leakage device. Thus, the extremely intricate and costly fabrication procedure may be difficult to justify for commercial consumer-grade applications. Nevertheless, if successful transfer or growth of the blue cell onto a lattice-matched R-G cell with proper alignment, coupled with the successful implementation of contacts, is achieved, these detectors are anticipated to surpass perovskites in terms of both performance and stability.

**Supplementary Table 4. Semiconductor compositions suitable for use in color detector layers amongst III-V semiconductors.**

| Composition | Target color | Band gap, eV | Substrate |
|---|---|---|---|
| $Ga_xIn_{x-1}P$ | R, G | 1.83-1.93[19],1.68-1.88[18]; 2.2-1.4 (pure InP) [33] | GaAs wafer[19] |
| AlxGa1-xAs | R, G | 1.42-2.16eV[34] | GaAs wafer[34] |
| $AlxGayIn_{1-x-y}P$ | G | 2.1[11] | GaAs |
| AlxGa1-xP | R, G | 2.33-1.4[33]; 2.31[35] | GaAs |
| InxGa1-xN | B | 2.8-1.7[36], 0.77-3.4[25], 3.5-1.7[37] | GaN, or GaN buffer |

### 2.2 Organic photodetectors

In contrast to III-V semiconductors and perovskites, organic semiconductors have received much attention as highly suitable materials for vertically stacked color sensors, primarily due to their exceptional spectral tunability. This tunability is achievable through molecular engineering, facilitating the development of photodetectors that are inherently sensitive to various spectral regions. Additionally, organic photodetectors are attractive for their manufacturability using low-temperature, solution-based techniques, such as printing[38,39] and spincoating[40,41], especially on flexible plastic substrates.

However, the fabrication of stacked organic photodetectors presents significant challenges. These include sputter damage incurred during the deposition of transparent conductive oxides[42-44], and the requirement to select orthogonal solvent mixtures for the deposition of color-sensitive layers to prevent dissolution of underlying layers[40,45,46]. In the case of thermally evaporated detectors, fabricating highly efficient devices poses significant challenges, primarily due to the inherent difficulties in forming bulk heterojunctions using a vapor deposition process[47,48]. Moreover, there is a notable scarcity of high-performance blue light detectors in the literature[49].

Despite these challenges, there have been successful demonstrations of integrating organic semiconductors with silicon chips, [41,50-52] including the development of stacked organic sensors[40,53-55]. There exist also reports about mechanically stacked triple-color organic detectors[56] of a single instance of a vertically stacked triple-color sensor using thin metal electrodes[57], likely utilised due to the technological difficulties associated with applying sputtered electrodes in organic photodetectors. This note seeks to evaluate these challenges and explore why a fully functional triple organic photodiode has yet to be reported, aiming to provide insights into the limitations and potential breakthroughs in this field.

*2.2.1 Color selectivity of organic sensors*

The color selectivity of organic sensors, particularly in the blue light spectrum, remains a challenging matter in the field of organic electronics. While numerous studies have focused on developing green[58-60] and broadband[8,61,62] organic detectors, the availability of organic materials suitable for blue light detection is comparatively limited. The most efficient blue detectors typically employ mixtures of $C_{60}$ or $C_{70}$ fullerene derivatives and donor molecules, such as rubrene[49,63] or PffBT4T-2OD(Poly[(5,6-difluoro-2,1,3-benzothiadiazol-4,7-diyl)-alt-(3,3’’’-di(2-octyldodecyl)-2,2’;5’,2’’;5’’,2’’’-quaterthiophen-5,5’’’-diyl)]) [64]. However, the absorption spectrum of C60 does not align well with the blue spectral region, leading to suboptimal color selectivity in such devices. For instance, in stacked sensors with blue and green channels, a 20% response to green light (500-600nm) was observed from the blue channel, likely due to the optical absorbance from the $PC_{61}BM$ ([6,6]-phenyl-C61-butyric acid methyl ester) layer[40]. An alternative strategy involves the use of homojunctions with blue-sensitive chromophores. A notable example of color selective mechanically stacked 3-layer sensor used Co-TTP (tetraphenylporphyrin) which exhibits an absorption maximum at 430 nm. This peak, however, falls short of covering the entire visible blue region, leading to color selectivity that is inferior to that of modern color-filter arrays[65]. Additionally, DPh-DNTT (diphenyl-dinaphtho[2,3-b:2′,3′-f]-thieno[3,2-b] thiophene) has been explored for blue light sensitivity, aiming to minimize the blue cell's response to green and red light, with an absorption edge at around 520 nm[54]. Despite these efforts, high levels of color crosstalk for blue light have been observed, attributed to the incomplete absorption by the blue-sensitive layer. Other notable approaches have included the use of pure F8BT (poly(9,9-di-n-octylfluorenyl-2,7-diyl)-co-1,4-benzo-(2,1,3)-thiadiazole) [66] or F8BT doped with DMTPS (1,1-dimethyl-2,3,4,5-tetraphenylsilole) [25]. Overall, aligning the absorption characteristics of organic

materials with their electronic properties sufficient for high-performance detectors may not be as straightforward as with perovskites. This complexity suggests that challenges in developing stacked organic sensors, particularly those with precise color selectivity, may impede rapid progress in this area.

*2.2.2 Transparent electrodes and sputter damage in organic photodetectors*

Sputtering is a plasma-assisted, physical vapor deposition method that involves the bombardment of a target material by high energy ions followed by deposition of the ejected particles onto a substrate. The sputtering processes are widely used for the fabrication of transparent conductive oxide electrodes that possess superior transparency and stability compared to thin metal electrodes[67]. However, a significant drawback of this technique is the sputtering damage inflicted on the underlying layers, attributable to the bombardment with highly energetic ions[43,67,68]. This issue is of particular concern for organic semiconductors, which are vulnerable to oxygen and are physically soft, rendering them sensitive to such damage[43]. As a result, many organic devices traditionally opt for metal or semitransparent metal electrodes, despite the compromise to the optical efficiency of stacked devices[57].

Recently, a growing interest is focused on semitransparent organic solar cells and photodetectors that incorporate transparent conductive oxides deposited atop the organic layer[44,55]. This interest is likely spurred by advancements in tandem perovskite solar cells, which encounter similar challenges related to sputter damage[69,70]. Additionally, less damaging transparent conductive oxide deposition methods can be used such as eclipse pulsed laser deposition, have demonstrated compatibility with organic solar cells (OSC), offering performance on par with metallic references [71]. Nonetheless, these methods are often expensive and require sophisticated equipment.

*2.2.3 Summary for organic photodetectors*

Unlike perovskites, where bandgap tunability is achieved through halide mixing, tuning the bandgap in organic materials requires altering the molecular composition, which can impose significant challenges on the fabrication of multiband detectors. The limited availability of high-performance vapor-deposited organic photosensitive films necessitates reliance on solution-processed detectors, introducing challenges related to solvent compatibility between layers. Moreover, the broad absorption profile of organic detectors may not be as advantageous for machine vision applications when compared to perovskites, as discussed in Supplementary Note

3, suggesting no direct benefit in terms of color accuracy enhancement over existing color filter arrays. On the other hand, organic materials do not suffer from ion migration[72], a significant concern for the stability of perovskite detectors. Despite the challenges, organic materials remain promising candidates for the development of stacked detectors, and their performance warrants comparison with perovskite technology as an alternative approach to multicolor pixel conception. Moreover, an important opportunity might arise from the monolithic integration of organic and perovskite layers in one archetecture, facilitated by the orthogonal solubility of perovskites and organic semiconductors in polar and non-polar solvents.

**Supplementary Note 3. Procedure for evaluation of color accuracy of optical sensor**

The color accuracy of the sensor has been tested under laboratory conditions that closely mimic the natural light reception process, allowing a quantitative evaluation. We used an optical stage (Fig. 3 a) where we positioned a light source, D50-equivalent with emission spectrum $W(\lambda)$ presented in Fig. 3 b (broadband white LED from LCFOCUS, FS-504, 10W, 380-780 nm), illuminating a translation stage with MacBeth ColorChecker with patches chart representing a standard color palette (the individual patches (*m*,*n*) are represented by albedo spectra $A_{m,n}(\lambda)$). The chart was masked with a black opaque stencil so that solely individual patches were illuminated. The reflected light is collimated and focused on the sample of perovskite stacked photodetectors. The photodetectors were operated under 0 V bias and the photocurrents from all 3 channels are measured. The color accuracy can be evaluated either through experimentally measured photocurrents or recalculated *via* measured EQE spectra. Both methods gave similar estimates. The latter method allows a direct comparison of the sensors of different technologies based on their spectral responsivity.

Theoretically, the values of the photocurrents (*i*=*R*, *G* ,*B*) may be represented as:

$$P_{i,m,n} = \int_{380nm}^{800nm} W(\lambda) A_{m,n}(\lambda)\, \mathrm{EQE_i}(\lambda) d\lambda \qquad \text{(S1).}$$

Alternatively, the photocurrent values are measured experimentally as presented in Fig. 3 a. The raw photocurrent values are corrected for background and cross-talk (10-15% for neighboring channels), normalized, linearized (corrected to the function $Argument^k$ , where $k$ = 0.4-0.6) or *i.e.* "grey-balanced" using 6 border patches with grey levels of the chart. To allocate the photocurrent signals (raw values of *RGB* channels) into a standard *XYZ* color space, they are to be renormalized with the transfer matrix:

$$\begin{matrix} X_{m.n} \\ Y_{m.n} \\ Z_{m.n} \end{matrix} = M_{i,j} \cdot \begin{matrix} P_{R,m.n} \\ P_{G,m.n} \\ P_{B,m.n} \end{matrix} \qquad \text{(S2)}$$

where the transfer matrix $M_{i,j}$ is specific for a particular image sensor and is calculated as:

$$M_{i,j} = \int_{380nm}^{800nm} CIE_{XYZ_i}(\lambda)\, \mathrm{EQE_j}(\lambda) d\lambda, \qquad \text{(S3)}$$

where CIE_$XYZ_i$ are human standard observer functions with $i$= $x$,$y$,$z$ and $j$=R,G,B channels of the sensor. For the correct calculation of the color accuracy the normalized *XYZ* values are transferred to CIELAB color space:

$$\varepsilon = 0.008856,\ \kappa = 903.3 \tag{S4}$$

$$fx = \begin{cases} \sqrt[3]{X} & if\ X > \varepsilon \\ \frac{\kappa X+16}{116} & otherwise \end{cases} \tag{S4}$$

$$fy = \begin{cases} \sqrt[3]{Y} & if\ Y > \varepsilon \\ \frac{\kappa Y+16}{116} & otherwise \end{cases} \tag{S5}$$

$$fz = \begin{cases} \sqrt[3]{Y} & if\ Y > \varepsilon \\ \frac{\kappa Y+16}{116} & otherwise \end{cases} \tag{S6}$$

$$L = 116fy - 16 \tag{S7}$$

$$a = 500(fx - fy) \tag{S8}$$

$$b = 200(fy - fz) \tag{S9}$$

In the CIELAB color space color error or color difference is calculated as mean variation of the 3-color coordinated from the reference color coordinates *Lab*_ref for the corresponding color patch over the whole chart:

$$\Delta E_{Lab} = \sum_{m,n} \sqrt{\left(L_{m,n} - L_{ref}{}_{m,n}\right)^2 + \left(a_{m,n} - a_{ref}{}_{m,n}\right)^2 + \left(b_{m,n} - b_{ref}{}_{m,n}\right)^2} \tag{S10}$$

Apparently, as smaller the *ΔLab* value for the particular color sensor are, the closer is the sensor to the ideal for color representation.

Finally, it is a good visual exercise to render back all the color values to the picture of the ColorChecker chart. Typically, it requires conversion of *XYZ* values to a standard *RGB* color space:

$$\begin{pmatrix} R \\ G \\ B \end{pmatrix} = M^{-1} \begin{pmatrix} X \\ Y \\ Z \end{pmatrix}, \quad \text{where } M = \begin{pmatrix} 0.412 & 0.358 & 0.18 \\ 0.213 & 0.715 & 0.072 \\ 0.019 & 0.119 & 0.950 \end{pmatrix} \tag{S11}$$

The comparison of the application of the above described algorithm for the sensor's sensitivity characteristics that correspond to Foveon, CFA, and stacked perovskite sensors is presented in

Extended Data Fig. 4. We note that the color representation, especially for Foveon-type sensors is far from adequate, so we suppose that commercial cameras utilize complicated proprietary postprocessing algorithms with “more aggressive” color cross-talk correction, use sensor-specific transfer matrises and gamma-corrections, etc.

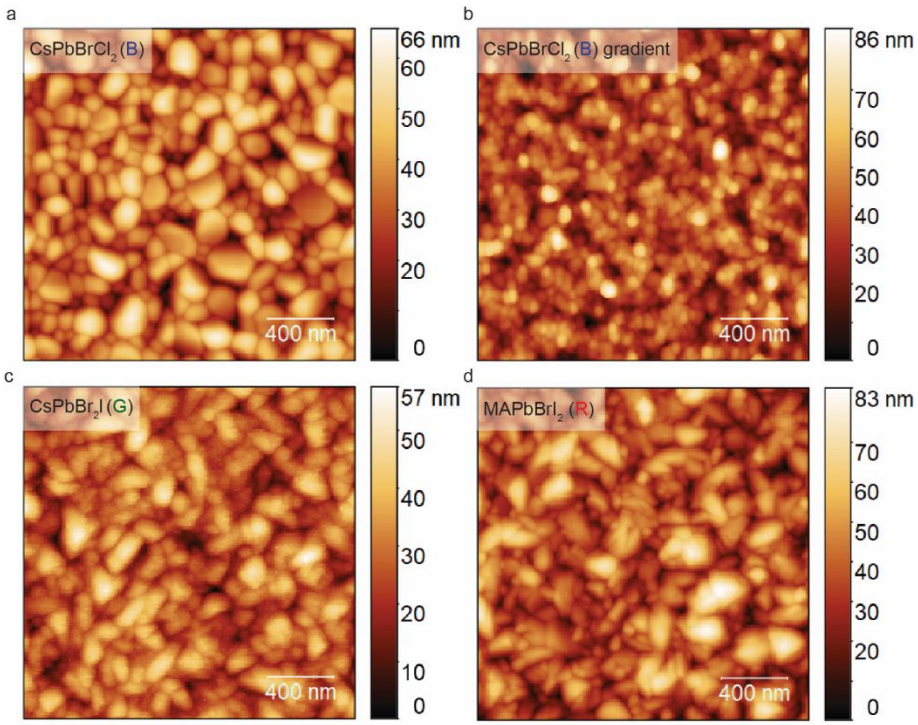


**Supplementary Fig. 1 | Atomic force microscopy images of perovskite layers.**
**a, b** $CsPbBrCl_2$ (B) **c.** $CsPbBr_2I$ (G), **d**. $MAPbBrI_2$ (R), in normal and gradient configurations, were deposited on substrates that mimic the configuration of a single-color detector stack, specifically ITO/ETL for G detectors, or ITO/HTL for R and B detectors. Scans were collected in tapping mode in normal and gradient configurations were deposited on substrates that mimic the configuration of a single-color detector stack, specifically ITO/ETL for G detectors, or ITO/HTL for R and B detectors. Scans were collected in tapping mode.

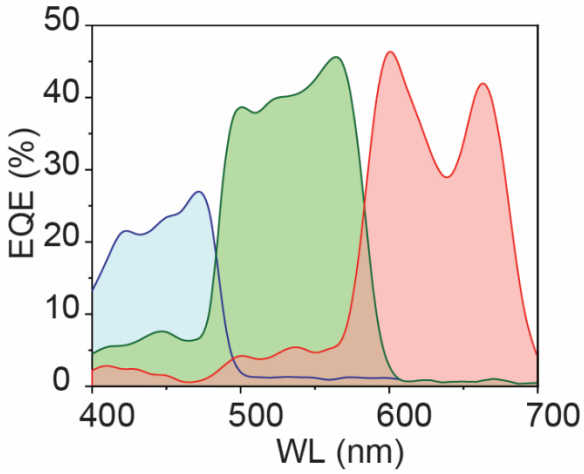


**Supplementary Fig. 2 | External Quantum Efficiency of a stacked detector with structure 1**. The 4-terminal structure contained $CsPbBrCl_2$ (B) $CsPbBr_2I$ (G) $MAPbBrI_2$ (R) based detectors sandwiched between charge transport layers. R and G layers are separated with $SnO_2/SiO_2$ dielectric layer.

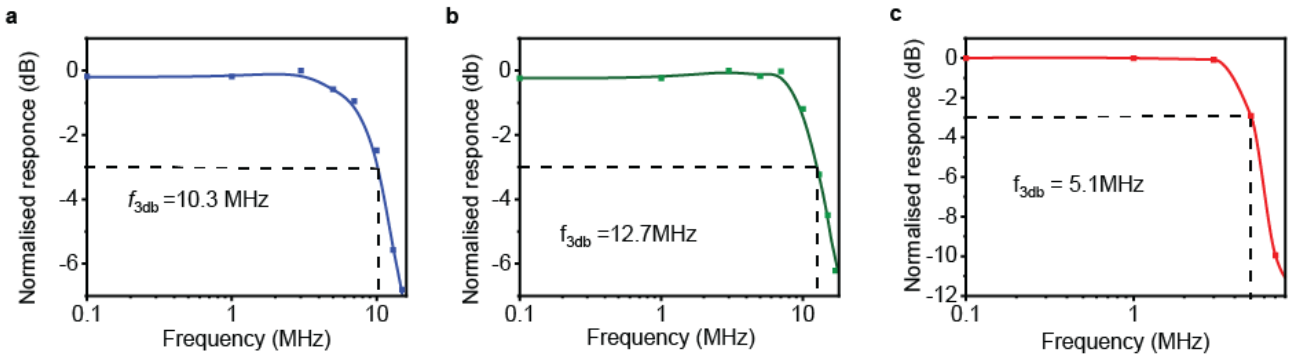


**Supplementary Fig. 3 | 3 dB bandwidth of the R, G, and B single color detectors.**
For these measurements, we fabricated smaller area (20x200µm) photodetectors to avoid RC-limited response. Additionally, we replaced the ITO layer with thin (30nm) gold. The detector responses were collected using a pico-second blue laser with a variable repetition rate.

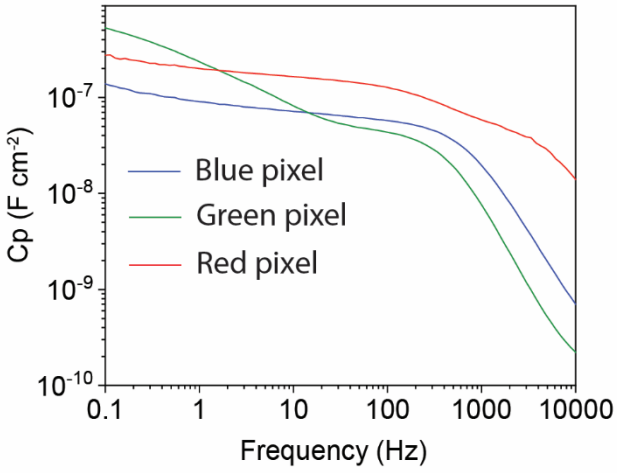


**Supplementary Fig. 4 | Capacitance vs frequency measurements of stacked photodetectors.** Capacitance was measured using impedance spectroscopy measurements and structure 1 pixel with 0.06 mm2 (B)|0.09 mm2 (G)|0.06 mm2 (B) detector area. The measurements were done under dark conditions.

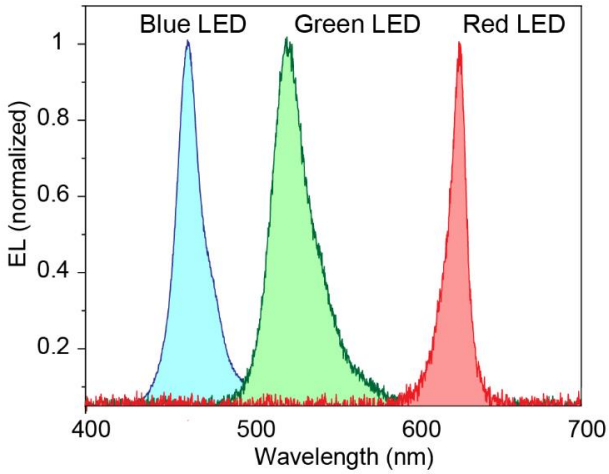


**Supplementary Fig. 5 | Emission spectra of RGB channels emitted by LC-10W diode.** The data were experimentally measured utilizing a Thorlabs fiber optics spectrometer coupled via an optical fiber to the emitting surface of the LED.

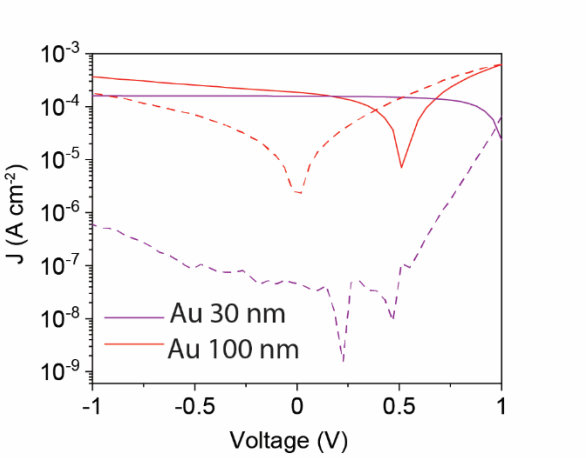


**Supplementary Fig. 6 | Comparative performance of red detectors with 30 nm and 100 nm bottom gold electrode.** The J-V (current-voltage) performance curves presented are derived from samples with detector structures identical to those of the red detectors, arranged in a stacked configuration.

## Supplementary References


1 Ruiz-Ruiz, M. *et al.* Real-time microscopy of the relaxation of a glass. *Nature Physics* **19**, 1509-1515 (2023).

2 Zhu, H. L. *et al.* Room-temperature solution-processed NiOx:PbI2 nanocomposite structures for realizing high-performance perovskite photodetectors. *ACS Nano* **10**, 6808-6815 (2016).

3 Sutherland, B. R. *et al.* Sensitive, fast, and stable perovskite photodetectors exploiting interface engineering. *ACS Photonics* **2**, 1117-1123 (2015).

4 Dou, L. *et al.* Solution-processed hybrid perovskite photodetectors with high detectivity. *Nature Communications* **5**, 5404 (2014).

5 *Thorlabs photodetectors webpage*, <https://www.thorlabs.com/newgrouppage9.cfm?objectgroup_id=285> (2024).

6 *Hamamatsu photodetectors webpage*, <https://www.hamamatsu.com/eu/en/product/optical-sensors/photodiodes/si-photodiodes/S12698-07.html> (2024).

7 Armin, A. *et al.* Narrowband light detection via internal quantum efficiency manipulation of organic photodiodes. *Nature Communications* **6**, 6343 (2015).

8 Xing, S. *et al.* Organic thin-film red-light photodiodes with tunable spectral response via selective exciton activation. *ACS Applied Materials & Interfaces* **12**, 13061-13067 (2020).

9 Tang, Z. *et al.* Polymer:fullerene bimolecular crystals for near-infrared spectroscopic photodetectors. *Advanced Materials* **29**, 1702184 (2017).

10 Geisz, J. F. *et al.* Six-junction III–V solar cells with 47.1% conversion efficiency under 143 Suns concentration. *Nature Energy* **5**, 326-335 (2020).

11 Dimroth, F. *et al.* Four-junction wafer-bonded concentrator solar cells. *IEEE Journal of Photovoltaics* **6**, 343-349 (2016).

12 Dimroth, F. *et al.* 3-6 junction photovoltaic cells for space and terrestrial concentrator applications. In *Conference Record of the Thirty-first IEEE Photovoltaic Specialists Conference, 2005.* 525-529.https://doi.org/10.1109/PVSC.2005.1488185

13 Chai, J. *et al.* High responsivity and high speed InGaN-based blue-light photodetectors on Si substrates. *RSC Adv* **11**, 25079-25083 (2021).

14 Liu, X. *et al.* High-bandwidth InGaN self-powered detector arrays toward MIMO visible light communication based on micro-LED arrays. *ACS Photonics* **6**, 3186-3195 (2019).

15 Currie, M. *et al.* High-speed high-responsivity low temperature grown GaAs detector. In *IEEE Photonics Conference 2012.* 312-313.https://doi.org/10.1109/IPCon.2012.6358617

16 Helmers, H. *et al.* Advancing solar energy conversion efficiency to 47.6% and exploring the spectral versatility of III-V photonic power converters. In *SPIE Photonics West: Physics, Simulation, and Photonic Engineering of Photovoltaic Devices XII.* 1288103 (2024).https://doi.org/10.1117/12.3000352

17 Haggren, T. *et al.* Strain-engineered multilayer epitaxial lift-off for cost-efficient III–V photovoltaics and optoelectronics. *ACS Applied Materials & Interfaces* **15**, 1184-1191 (2023).

18 Dimroth, F. *et al.* Metamorphic GayIn1-yP/ Ga1-xInxAs tandem solar cells for space and for terrestrial concentrator applications at C>1000 suns. *Prog. Photovolt.: Res. Appl.* **9**, 165-178 (2001).
19 Park, K. W., Park, C. Y. & Lee, Y. T. Band gap tunability of molecular beam epitaxy grown lateral composition modulated GaInP structures by controlling V/III flux ratio. *Applied Physics Letters* **101**, 051903 (2012).
20 Merrill, J. & Senft, D. C. Directions and materials challenges in high-performance photovoltaics. *JOM* **59**, 26-30 (2007).
21 Akimoto, K. *et al.* Photoluminescence killer center in AlGaAs grown by molecular-beam epitaxy. *Journal of Applied Physics* **59**, 2833-2836 (1986).
22 Parmar, M. & Reeves, S. J. Selection of optimal spectral sensitivity functions for color filter arrays. In *2006 International Conference on Image Processing.* 1005-1008 (2006).https://doi.org/10.1109/ICIP.2006.312669
23 Wu, J. When group-III nitrides go infrared: new properties and perspectives. *Journal of Applied Physics* **106**, 011101 (2009).
24 Wu, J. *et al.* Unusual properties of the fundamental band gap of InN. *Applied Physics Letters* **80**, 3967-3969 (2002).
25 Kour, R. *et al.* Recent advances and challenges in Indium Gallium Nitride (InxGa1-xN) materials for solid state lighting. *ECS Journal of Solid State Science and Technology* **9** (2019).
26 Schley, P. *et al.* Dielectric function and van hove singularities for In-rich InxGa1-xN alloys: comparison of N- and metal-face materials. *Physical Review B* **75**, 205204 (2007).
27 Jones, R. E. *et al.* Evidence for p-Type Doping of InN. *Physical Review Letters* **96**, 125505 (2006).
28 Ohsawa, J., Kozawa, T., Ishiguro, O. & Itoh, H. Selective detection of blue and ultraviolet light by an InGaN/GaN schottky barrier photodiode. *Japanese Journal of Applied Physics* **45**, L614 (2006).
29 Chiou, Y.-Z. *et al.* InGaN/GaN MQW p–n junction photodetectors. *Solid-State Electronics* **46**, 2227-2229 (2002).
30 Kang, C.-M. *et al.* Monolithic integration of AlGaInP-based red and InGaN-based green LEDs via adhesive bonding for multicolor emission. *Scientific Reports* **7**, 10333 (2017).
31 Zhang, S., Wang, H., Wang, H. & Jiang, H. InGaN/GaN MQWs green-light photodetectors with thin GaN barrier layers. In *Applied Optics and Photonics China (AOPC2019).* 1133403 (SPIE, 2019).https://doi.org/http://dx.doi.org/10.1117/12.2539045
32 Ager, J. W. *et al.* InGaN/Si heterojunction tandem solar cells. In *2008 33rd IEEE Photovoltaic Specialists Conference.* 1-5 (IEEE, 2008).https://doi.org/10.1109/PVSC.2008.4922663
33 Vaisman, M. *et al.* Direct-gap 2.1–2.2 eV AlInP solar cells on GaInAs/GaAs metamorphic buffers. *IEEE Journal of Photovoltaics* **6**, 571-577 (2016).
34 Ben Slimane, A. *et al.* 1.73 eV AlGaAs/InGaP heterojunction solar cell grown by MBE with 18.7% efficiency. *Progress in Photovoltaics* **28**, 393-402 (2020).
35 Zhao, S. *et al.* AlInP photodiode x-ray detectors. *Journal of Physics D: Applied Physics* **52**, 225101 (2019).

36 Emanuel Thomet, J. *et al.* Bandgap engineering of indium gallium nitride layers grown by plasma-enhanced chemical vapor deposition. *J. Vac. Sci. Technol. A* **40** (2022).
37 Perlin, P. *et al.* Influence of pressure on the optical properties of InxGa1-xN epilayers and quantum structures. *Physical Review B* **64**, 115319 (2001).
38 Azzellino, G. *et al.* Fully inkjet-printed organic photodetectors with high quantum yield. *Advanced Materials* **25**, 6829-6833 (2013).
39 Lee, S.-H. *et al.* Toward color-selective printed organic photodetectors for high-resolution image sensors: From fundamentals to potential commercialization. *Materials Science and Engineering: R: Reports* **147**, 100660 (2022).
40 Zhao, T., Xia, K., Natali, D. & Pecunia, V. Solution-based integration of vertically stacked organic photodetectors toward easy-to-fabricate filterless multi-color light sensors. *Advanced Optical Materials* **10**, 2200862 (2022).
41 Baierl, D. *et al.* A hybrid CMOS-imager with a solution-processable polymer as photoactive layer. *Nature Communications* **3**, 1175 (2012).
42 Wu, J.-L. *et al.* Top-Illuminated organic photodetectors beyond 1000 nm wavelength response enabled by a well-defined Interfacial engineering. *Advanced Optical Materials* **10**, 2101723 (2022).
43 Suemori, K. Assessment of sputtering damage in organic layer surface based on energy distribution of positively charged particles formed during facing-target sputtering of indium–tin oxide. *Organic Electronics* **116**, 106764 (2023).
44 Kim, D.-H. *et al.* A high performance semitransparent organic photodetector with green color selectivity. *Applied Physics Letters* **105** (2014).
45 Liu, H. *et al.* Orthogonal solvent-sequential deposition of a nonfullerene acceptor solution on polymer donor film: complete interpenetration and highly efficient inverted organic solar cells. *Journal of Materials Chemistry A* **11**, 19860-19869 (2023).
46 Gaikwad, A. M. *et al.* Identifying orthogonal solvents for solution processed organic transistors. *Organic Electronics* **30**, 18-29 (2016).
47 Kovacik, P., Assender, H. E. & Watt, A. A. R. Morphology control in co-evaporated bulk heterojunction solar cells. *Solar Energy Materials and Solar Cells* **117**, 22-28 (2013).
48 Riede, M. *et al.* Efficient organic tandem solar cells based on small molecules. *Advanced Functional Materials* **21**, 3019-3028 (2011).
49 Zhang, T. *et al.* High-performance filterless blue narrowband organic photodetectors. *Advanced Functional Materials* **34**, 2308719 (2024).
50 Lim, S.-J. *et al.* Organic-on-silicon complementary metal–oxide–semiconductor colour image sensors. *Scientific Reports* **5**, 7708 (2015).
51 Shekhar, H. *et al.* Hybrid image sensor of small molecule organic photodiode on CMOS – integration and characterization. *Scientific Reports* **10**, 7594 (2020).
52 Bulliard, X. *et al.* Dipolar donor–acceptor molecules in the cyanine limit for high efficiency green-light-selective organic photodiodes. *Journal of Materials Chemistry C* **4**, 1117-1125 (2016).
53 Aihara, S. *et al.* Stacked image sensor with green- and red-sensitive organic photoconductive films applying zinc oxide thin-film transistors to a signal readout circuit. *IEEE Transactions on Electron Devices* **56**, 2570-2576 (2009).

54 Sakai, T. *et al.* Color-filter-free three-layer-stacked image sensor using blue/green-selective organic photoconductive films with thin-film transistor circuits on CMOS image sensors. *ACS Applied Electronic Materials* **3**, 3085-3095 (2021).
55 Park, S. *et al.* Transparent organic photodiodes for high-detectivity CMOS image sensors. *Optica* **9**, 992-999 (2022).
56 Takagi, T. *et al.* Image sensor with organic photoconductive films by stacking red/green and blue components. *Electronic Imaging* **28**, 1-4 (2016).
57 Nasrollahi, B., Jailani, J. M., Zhao, T. & Pecunia, V. Printable organic photodetectors with gain toward high-performance vertically stacked color sensors. *IEEE Journal on Flexible Electronics* **2**, 285-292 (2023).
58 Lim, Y. *et al.* Green-light-selective organic photodiodes with high detectivity for CMOS color image sensors. *ACS Applied Materials & Interfaces* **12**, 51688-51698 (2020).
59 Guo, H. *et al.* Unsymmetric squaraine for narrow band green-selective organic photodetectors. *Organic Electronics* **92**, 106122 (2021).
60 Lee, G. H. *et al.* Green-light-selective organic photodiodes for full-color imaging. *Opt. Express* **27**, 25410-25419 (2019).
61 Li, N., Eedugurala, N., Azoulay, J. D. & Ng, T. N. A filterless organic photodetector electrically switchable between visible and infrared detection. *Cell Reports Physical Science* **3** (2022).
62 Liu, J. *et al.* Challenges and recent advances in photodiodes-based organic photodetectors. *Phys. Chem. Chem. Phys.* **51**, 475-503 (2021).
63 Li, W. *et al.* Squarylium and rubrene based filterless narrowband photodetectors for an all-organic two-channel visible light communication system. *Organic Electronics* **37**, 346-351 (2016).
64 Lu, J. H. *et al.* High-performance organic photodiodes for blue-light hazard detection. *Chemical Engineering Journal* **437**, 135327 (2022).
65 Seo, H. *et al.* Color sensors with three vertically stacked organic photodetectors. *Japanese Journal of Applied Physics* **46**, L1240 (2007).
66 Fukuda, T. *et al.* Improved optical-to-electrical conversion efficiency by doping silole derivative with low ionization potential. *Physical Status Solidi A* **209**, 2324-2329 (2012).
67 Aydin, E. *et al.* Sputtered transparent electrodes for optoelectronic devices: Induced damage and mitigation strategies. *Matter* **4**, 3549-3584 (2021).
68 Ellmer, K. & Welzel, T. Reactive magnetron sputtering of transparent conductive oxide thin films: Role of energetic particle (ion) bombardment. *Journal of Materials Research* **27**, 765-779 (2012).
69 Reddy, S. H. *et al.* Holistic approach toward a damage-less sputtered indium tin oxide barrier layer for high-stability inverted perovskite solar cells and modules. *ACS Applied Materials & Interfaces* **14**, 51438-51448 (2022).
70 Liu, K. *et al.* Reducing sputter induced stress and damage for efficient perovskite/silicon tandem solar cells. *Journal of Materials Chemistry A* **10**, 1343-1349 (2022).
71 Schubert, S. *et al.* Eclipse pulsed laser deposition for damage-free preparation of transparent ZnO electrodes on top of organic solar cells. *Advanced Functional Materials* **25**, 4321-4327 (2015).

72 Sakhatskyi, K. *et al.* Assessing the drawbacks and benefits of ion migration in lead halide perovskites. *ACS Energy Letters* **7**, 3401-3414 (2022).